Dynamic Modeling Based on Coupled Modes for Wireless Power Transfer Systems

Hongchang Li, *Student Member, IEEE*, Kangping Wang, *Student Member, IEEE*, Lang Huang, *Student Member, IEEE*, Wenjie Chen, *Member, IEEE*, and Xu Yang, *Member, IEEE*

***Abstract*—A novel dynamic modeling method based on the concept of coupled modes is proposed for wireless power transfer (WPT) systems which use magnetic resonant coupling. The proposed method aims on the dynamics of the overall WPT system, including the nonlinear inverter and rectifier. It uses the slowly varying amplitudes and phases of coupled modes rather than resonant currents and voltages to describe the coupled resonances. Three analytical models—averaged model, small signal model, and conductance network model are developed sequentially by using the proposed method. The orders of the developed models are equal to or lower than that of the discrete state space model. In contrast, the existing dynamic modeling methods for WPT systems and resonant converters have to transform the discrete state space model into a higher order model or use complex currents and voltages in order to adopt the averaging method and obtain an analytical model. Simulation and experimental results give a firm support to the proposed method and models. The concept employed in this paper provides a deeper insight into the dynamic behaviors of coupled resonances.**

***Index Terms*—Averaged model, conductance network model, coupled modes, small signal model, wireless power transfer.**

I. Introduction

WIRELESS power transfer (WPT) using magnetic resonant coupling is becoming one of the most attractive technologies to achieve near-field wireless transmission of energy [1]. With a good tradeoff between power transfer distance and efficiency, this technology is preferred in many daily and industrial applications, such as wireless power supplies/chargers for cellphones [2], electric vehicles [3]–[7], and biomedical implants [8]–[11].

Generally, WPT systems are desired to provide stable output voltage as power supplies. Unfortunately, the output voltage of an open-loop WPT system depends strongly on the system's parameters, e.g., coupling coefficient and load impedance [12], [13]. Various control schemes have been investigated to maintain constant output voltage against parameter variations [8], [11], [14]–[18]. Most of these control schemes are based on the static characteristics of the WPT systems. However, a dynamic model is needed to design a controller in the applications, which require rapid startup or regulation. One example of such kind of application is the WPT system for online electric vehicles [6], [7]. Wireless powering systems for household appliances and smart devices also require rapid regulation when they are powered without batteries. Besides, a dynamic model can help to investigate the maximum stresses during startup and shutdown processes, which may be several times higher than the steady state stresses.

Modeling the dynamics of the coupled resonant tank in a WPT system is not difficult since it is a linear time-invariant (LTI) network. The conventional state space models of two resonant tanks are developed in [19] and [20], respectively. However, the nonlinear components (i.e., inverter and rectifier) are not taken into account. Therefore, the closed form analytical expression of dc-to-dc or control-to-output dynamic characteristics cannot be derived out.

Things become complex when modeling a whole WPT system from source to load, including the inverter and rectifier. Fortunately, the modeling methods for resonant converters developed over the past decades also apply to WPT systems. The generalized state space averaging method proposed by Sanders *et al.* is adopted in [6] and [21]. The extended describing functions technique is applied in [22]. Laplace phasor transform is used in [7]. All these methods that accurately describe the nonlinear dynamics of WPT systems share the same concept: using two slowly varying state variables to describe a fast varying state variable which is approximately sinusoidal. As a result, these methods increase the model's order compared with the discrete state space model or use complex currents and voltages.

To overcome the higher order problem and make a straightforward real dynamic model from the energy point of view, this paper describes the loosely coupled resonances using the concept of coupled modes. This concept can be found in coupled-mode theory (CMT) [23]. Actually, CMT has already been used to analyze WPT systems by Kurs *et al.* [24]. However, only the steady-state characteristics such as efficiency and field strength are investigated in [24]. The obstacle to use CMT to develop a dynamic model of WPT system is that the resonant frequencies of the coupled resonances are not identical in practice for some reasons [17], [25] and it violates the condition of CMT. In this paper, the phases of the modes are considered so that the coupled-mode description applies to the cases in which the frequencies are not identical. Each of the resonances is described by two real variables: mode amplitude and phase. The continuous dynamic equations of the coupled modes are derived out

Manuscript received July 16, 2014; revised October 21, 2014; accepted November 18, 2014. Date of publication November 26, 2014; date of current version July 10, 2015. This work was supported by the National Natural Science Foundation of China under Project 51177129. Recommended for publication by Associate Editor J. M. Miller.

The authors are with the School of Electrical Engineering, Xi'an Jiaotong University, Xi'an, Shaanxi 710049, China (e-mail: hongchangli@stu.xjtu.edu.cn; wangkangping@stu.xjtu.edu.cn; trooper2013@stu.xjtu.edu.cn; cwj@mail.xjtu.edu.cn; yangxu@mail.xjtu.edu.cn).

Color versions of one or more of the figures in this paper are available online at http://ieeexplore.ieee.org.

Digital Object Identifier 10.1109/TPEL.2014.2376474

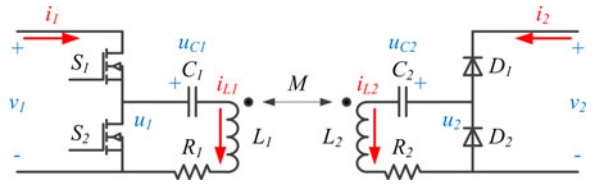

Fig. 1. Schematic diagram of a half-bridge type WPT stage.

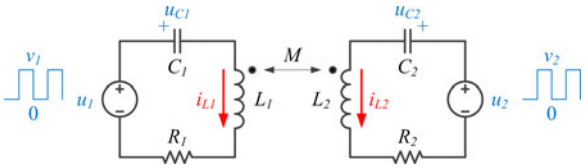

Fig. 2. Equivalent circuit of the ac part.

from the discrete state space model and the order of the derived equations is equal to that of the state space model. In addition, we propose a conductance network model to further reduce the order.

The rest of the paper is organized as follows: Section II proposes the modeling method based on coupled modes for a WPT stage which is abstracted out from WPT systems. Section III sequentially develops the averaged model, small signal model, and conductance network model of the WPT stage. The developed models are applied in system level modeling in Section IV and validated in Section V. Finally, the conclusion is shown in Section VI.

II. From State Space to Coupled Modes

A. Discrete State Space Model of WPT Stage

When we start to think of a WPT system as a power supply, it can be found that the key component in the system is the WPT stage which achieves dc-to-dc transmission of energy. Fig. 1 shows a half-bridge type WPT stage with series resonant tanks. In a WPT system, this stage may be connected with filters, power factor correction stage, or other conversion stages.

Our modeling starts from the WPT stage since the rest components in a WPT system have been well investigated in other kinds of power supplies. We assume that the input voltage of the WPT stage is v_1 and the output voltage is v_2, while switches S_1 and S_2 (power MOSFETs) are conducting alternately, a square waveform u_1 is obtained to drive the coupled resonant tanks. Similarly, while power diodes D_1 and D_2 are conducting alternately, a square waveform u_2 is generated to absorb the energy. Fig. 2 shows the equivalent circuit of the ac part.

In Fig. 2, we use effective inductances L_1 and L_2, effective capacitances C_1 and C_2, equivalent series resistances (ESR) R_1 and R_2, and mutual inductance M to model the coupled resonant tanks. u_1 and u_2 are considered as exciting source and sink, respectively. The dynamics of this equivalent circuit can

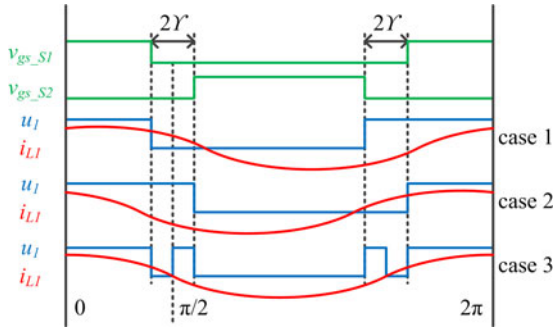

Fig. 3. Waveforms of drive signals, u_1 and i_{L1} at three cases.

be fully described by the discrete state space model as follows:

$$\begin{cases} L_1 \frac{di_{L1}}{dt} + M \frac{di_{L2}}{dt} + u_{C1} + R_1 i_{L1} = u_1 \\ C_1 \frac{du_{C1}}{dt} = i_{L1} \\ L_2 \frac{di_{L2}}{dt} + M \frac{di_{L1}}{dt} + u_{C2} + R_2 i_{L2} = u_2 \\ C_2 \frac{du_{C2}}{dt} = i_{L2} \end{cases} \tag{1}$$

where i_{L1} and i_{L2} are the resonant currents; u_{C1} and u_{C2} are the voltages across the capacitors.

We can solve (1) immediately when u_1 and u_2 are given. Fig. 3 shows the waveform of u_1 at three different operation cases, as well as i_{L1} and the gate drive signals of S_1 and S_2 (v_{gs_S1} and v_{gs_S2}). Fig. 3 also considers the dead time T_d between the drive signals. The phase of u_1 relative to v_{gs_S1} depends on the phase of i_{L1}, which always changes between positive and negative values in the dynamic process of the WPT stage. Therefore, we use v_{gs_S1} as the time reference to define u_1

$$u_1 = \begin{cases} \dfrac{\operatorname{sgn}(\cos\omega_s t) + 1}{2} v_1 & , |\cos\omega_s t| \geq \left|\cos\left(\frac{\pi}{2} - \gamma\right)\right| \\ \dfrac{-\operatorname{sgn}(i_{L1}) + 1}{2} v_1 & , |\cos\omega_s t| < \left|\cos\left(\frac{\pi}{2} - \gamma\right)\right| \end{cases} \tag{2}$$

where ω_s is the angular switching frequency of S_1 and S_2 and γ is the angle that corresponds to half of the dead time

$$\gamma = \frac{\omega_s T_d}{2}. \tag{3}$$

Both ω_s and γ are considered as constants rather than variables. The reasons are 1) ω_s should be equal (or very close) to the resonant frequency of L_2 and C_2 in order to achieve the highest energy efficiency, and 2) zero-voltage-switching (ZVS) of S_1 and S_2 can be achieved only in a small range of γ. From the efficiency point of view, ω_s and γ should equal their optimum values respectively and remain constant in operation. Comparatively, u_2 depends only on the direction of i_{L2} and is given by

$$u_2 = \frac{-\operatorname{sgn}(i_{L2}) + 1}{2} v_2. \tag{4}$$

In addition, full-bridge type WPT stage can also be described by (1), while we need to make some changes in (2) and (4) by multiplying the right hand expressions with 2.

B. Modeling WPT Stage by Coupled Modes

The state space model that accurately describes the circuit dynamics is intractable because of the nonlinearity, discontinuity, and time-variance. Even worse, the state space averaging method does not apply to (1) because of the fast varying state variables.

To overcome these problems, we model the WPT stage with the concept taken from CMT according to which the state of coupled resonances can be represented by coupled modes

$$\boldsymbol{a_n} = a_n e^{j(\omega_s t+\theta_n)} \tag{5}$$

where the indices denote the different resonators. The variables a_n are defined so that the energy contained in resonator n is a_n^2 [24]. In addition, we define the variables θ_n as the phases of the modes so that (5) applies to the coupled resonances which have different resonant frequencies. Both a_n and θ_n vary slowly with time.

In order to determine the dynamic equations of the coupled modes, we find the relationship between the coupled modes and the variables in (1) as follows.

Based on CMT, the modes are considered as energy orthogonal when the resonances are loosely coupled. Therefore, the resonant currents and voltages can be represented as (6) from the energy point of view

$$\begin{cases} i_{Ln} &= \sqrt{\frac{2}{L_n}} \cdot a_n \cos(\omega_s t+\theta_n) \\ u_{Cn} &= \sqrt{\frac{2}{C_n}} \cdot a_n \sin(\omega_s t+\theta_n). \end{cases} \tag{6}$$

According to (6), we can write out the derivatives of the resonant currents and voltages as

$$\begin{cases} \frac{di_{Ln}}{dt} = \sqrt{\frac{2}{L_n}} \left[\frac{da_n}{dt}\cos(\omega_s t+\theta_n) \right. \\ \qquad \left. - a_n\left(\omega_s + \frac{d\theta_n}{dt}\right)\sin(\omega_s t+\theta_n)\right] \\ \frac{du_{Cn}}{dt} = \sqrt{\frac{2}{C_n}} \left[\frac{da_n}{dt}\sin(\omega_s t+\theta_n) \right. \\ \qquad \left. + a_n\left(\omega_s + \frac{d\theta_n}{dt}\right)\cos(\omega_s t+\theta_n)\right]. \end{cases} \tag{7}$$

Furthermore, u_1 and u_2 are also represented with θ_n ($n = 1$, 2) according to (2) and (4)

$$\begin{cases} u_1 = \dfrac{\mathrm{sgn}[\cos(\omega_s t-\gamma \mathrm{sgn}\theta_1)]}{2} v_1 \\ u_2 = \dfrac{-\mathrm{sgn}[\cos(\omega_s t+\theta_2)]+1}{2} v_2. \end{cases} \tag{8}$$

The expression of u_1 in (8) is a little bit different from (2) when $-\gamma < \theta_1 < \gamma$ (case 3 of Fig. 3). However, the difference only exists during the dead time. From the energy point of view, this difference is not significant because i_{L1} crosses zero during the dead time when $-\gamma < \theta_1 < \gamma$ and the absolute value of i_{L1} is very small near the crossover point.

By substituting (6)–(8) into (1), the state variables i_{Ln} and u_{Cn} are replaced by a_n and θ_n and the dynamic equations of the coupled modes (their amplitudes and phases) are derived out from the state space model

$$\begin{aligned} \frac{da_1}{dt} =\ & \omega_1 a_1 \sin(\omega_s t+\theta_1)\cos(\omega_s t+\theta_1) \\ & + \frac{\sqrt{L_1/2}}{L_1L_2-M^2}\cos(\omega_s t+\theta_1) \\ & \times \left[-L_2\sqrt{\frac{2}{C_1}}a_1\sin(\omega_s t+\theta_1)\right. \\ & - L_2R_1\sqrt{\frac{2}{L_1}}a_1\cos(\omega_s t+\theta_1) \\ & + L_2\frac{\mathrm{sgn}[\cos(\omega_s t-\gamma\mathrm{sgn}\theta_1)]+1}{2}v_1 \\ & + MR_2\sqrt{\frac{2}{L_2}}a_2\cos(\omega_s t+\theta_2) \\ & + M\sqrt{\frac{2}{C_2}}a_2\sin(\omega_s t+\theta_2) \\ & \left. - M\frac{-\mathrm{sgn}[\cos(\omega_s t+\theta_2)]+1}{2}v_2\right] \end{aligned} \tag{9a}$$

$$\begin{aligned} \frac{d\theta_1}{dt} =\ & -\omega_s+\omega_1-\omega_1\sin^2(\omega_s t+\theta_1) \\ & - \frac{\sqrt{L_1/2}}{L_1L_2-M^2}\frac{\sin(\omega_s t+\theta_1)}{a_1} \\ & \times \left[-L_2\sqrt{\frac{2}{C_1}}a_1\sin(\omega_s t+\theta_1)\right. \\ & - L_2R_1\sqrt{\frac{2}{L_1}}a_1\cos(\omega_s t+\theta_1) \\ & + L_2\frac{\mathrm{sgn}[\cos(\omega_s t-\gamma\mathrm{sgn}\theta_1)]+1}{2}v_1 \\ & + MR_2\sqrt{\frac{2}{L_2}}a_2\cos(\omega_s t+\theta_2) \\ & + M\sqrt{\frac{2}{C_2}}a_2\sin(\omega_s t+\theta_2) \\ & \left. - M\frac{-\mathrm{sgn}[\cos(\omega_s t+\theta_2)]+1}{2}v_2\right] \end{aligned} \tag{9b}$$

$$\begin{aligned} \frac{da_2}{dt} =\ & \omega_2 a_2 \sin(\omega_s t+\theta_2)\cos(\omega_s t+\theta_2) \\ & + \frac{\sqrt{L_2/2}}{L_1L_2-M^2}\cos(\omega_s t+\theta_2) \\ & \times \left[-L_1\sqrt{\frac{2}{C_2}}a_2\sin(\omega_s t+\theta_2)\right. \\ & + L_1\frac{-\mathrm{sgn}[\cos(\omega_s t+\theta_2)]+1}{2}v_2 \\ & + MR_1\sqrt{\frac{2}{L_1}}a_1\cos(\omega_s t+\theta_1) \end{aligned}$$

$$+M\sqrt{\frac{2}{C_1}}a_1\sin(\omega_s t+\theta_1) - M\frac{\mathrm{sgn}[\cos(\omega_s t-\gamma\mathrm{sgn}\theta_1)]+1}{2}v_1\Big] \quad (9c)$$

$$\frac{d\theta_2}{dt} = -\omega_s+\omega_2-\omega_2\sin^2(\omega_s t+\theta_2) - \frac{\sqrt{L_2/2}}{L_1L_2-M^2}\frac{\sin(\omega_s t+\theta_2)}{a_2} \times\Big[-L_1\sqrt{\frac{2}{C_2}}a_2\sin(\omega_s t+\theta_2) - L_1R_2\sqrt{\frac{2}{L_2}}a_2\cos(\omega_s t+\theta_2) + L_1\frac{-\mathrm{sgn}[\cos(\omega_s t+\theta_2)]+1}{2}v_2 + MR_1\sqrt{\frac{2}{L_1}}a_1\cos(\omega_s t+\theta_1) + M\sqrt{\frac{2}{C_1}}a_1\sin(\omega_s t+\theta_1) - M\frac{\mathrm{sgn}[\cos(\omega_s t-\gamma\mathrm{sgn}\theta_1)]+1}{2}v_1\Big]. \quad (9d)$$

III. Analytical Models of the WPT Stage

A. Averaged Model

Assuming the slowly varying variables in (9)—a_n, θ_n, and v_n ($n=1,2$) are constant during a switching period, we eliminate the high-frequency terms such as $\omega_1 a_1\sin(\omega_s t+\theta_1)\cos(\omega_s t+\theta_1)$ by taking the average values of both sides of (9), while the low-frequency characteristics remain in the averaged equations, i.e., the time-invariant averaged model

$$\frac{da_1}{dt} = \frac{\sqrt{L_1/2}}{L_1L_2-M^2}\Big[-\frac{L_2R_1}{\sqrt{2L_1}}a_1-\frac{M}{\sqrt{2C_2}}a_2\sin(\theta_1-\theta_2) + \frac{MR_2}{\sqrt{2L_2}}a_2\cos(\theta_1-\theta_2)+\frac{L_2}{\pi}v_1 \times\cos(\theta_1+\gamma\mathrm{sgn}\theta_1)+\frac{M}{\pi}v_2\cos(\theta_1-\theta_2)\Big] \quad (10a)$$

$$\frac{d\theta_1}{dt} = -\omega_s+\frac{\omega_1}{2}-\frac{\sqrt{L_1/2}}{(L_1L_2-M^2)\,a_1}\Big[-\frac{L_2}{\sqrt{2C_1}}a_1 + \frac{M}{\sqrt{2C_2}}a_2\cos(\theta_1-\theta_2)+\frac{MR_2}{\sqrt{2L_2}}a_2\sin(\theta_1-\theta_2) + \frac{L_2}{\pi}v_1\sin(\theta_1+\gamma\,\mathrm{sgn}\,\theta_1)+\frac{M}{\pi}v_2\sin(\theta_1-\theta_2)\Big] \quad (10b)$$

$$\frac{da_2}{dt} = \frac{\sqrt{L_2/2}}{L_1L_2-M^2}\Big[-\frac{L_1R_2}{\sqrt{2L_2}}a_2+\frac{M}{\sqrt{2C_1}}a_1\sin(\theta_1-\theta_2) + \frac{MR_1}{\sqrt{2L_1}}a_1\cos(\theta_1-\theta_2) - \frac{L_1}{\pi}v_2-\frac{M}{\pi}v_1\cos(\theta_2+\gamma\mathrm{sgn}\theta_1)\Big] \quad (10c)$$

$$\frac{d\theta_2}{dt} = -\omega_s+\frac{\omega_2}{2}-\frac{\sqrt{L_2/2}}{(L_1L_2-M^2)\,a_2}\Big[-\frac{L_1}{\sqrt{2C_2}}a_2 + \frac{M}{\sqrt{2C_1}}a_1\cos(\theta_1-\theta_2)-\frac{MR_1}{\sqrt{2L_1}}a_1\sin(\theta_1-\theta_2) - \frac{M}{\pi}v_1\sin(\theta_2+\gamma\ \mathrm{sgn}\ \theta_1)\Big] \quad (10d)$$

where ω_n ($n=1,2$) is the angular resonant frequency of resonator *n*

$$\omega_n = \frac{1}{\sqrt{L_nC_n}}. \quad (11)$$

Let us represent the averaged model by a more concise form

$$\frac{d\boldsymbol{x}}{dt} = \boldsymbol{f}(\boldsymbol{x}, v_1, v_2) \quad (12)$$

where

$$\boldsymbol{x} = \begin{bmatrix} a_1 \\ \theta_1 \\ a_2 \\ \theta_2 \end{bmatrix} \quad (13)$$

$$\boldsymbol{f} = \begin{bmatrix} f_1 \\ f_2 \\ f_3 \\ f_4 \end{bmatrix} \quad (14)$$

and f_n ($n=1\ldots4$) is the right-hand side expression of the *n*th equation in (10). The order of the averaged model is the same as that of the state space model.

The equivalent circuit of the averaged model is shown in Fig. 4, where the WPT stage is considered as a two-port network. The external characteristics can be described by

$$\begin{cases} i_1 = g_1(\boldsymbol{x}) = \dfrac{1}{\pi}\sqrt{\dfrac{2}{L_1}}a_1\cos(\theta_1+\gamma\mathrm{sgn}\theta_1) \\ i_2 = g_2(\boldsymbol{x}) = -\dfrac{1}{\pi}\sqrt{\dfrac{2}{L_2}}a_2 \end{cases} \quad (15)$$

where i_1 and i_2 are the averaged port currents during a switching period.

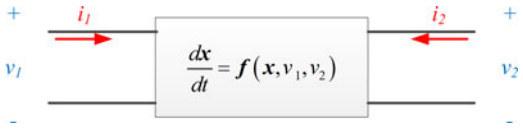

Fig. 4. Equivalent circuit of the averaged model.

B. Small Signal Model

The averaged model is continuous and differentiable in the two segments: $\theta_1>0$ and $\theta_1<0$, respectively, and can be

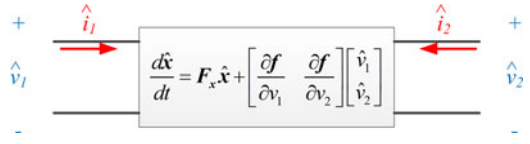

Fig. 5. Equivalent circuit of the small signal model.

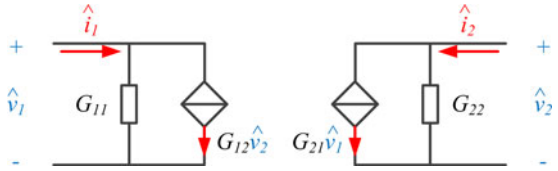

Fig. 6. Equivalent circuit of the conductance network model.

linearized locally according to the sign of θ_1. Supposing the small signals of the state variables and the input and output voltages are $\hat{a}_n$, $\hat{\theta}_n$, and $\hat{v}_n$ $(n = 1, 2)$, we can write out the linearized small signal model of the WPT stage as

$$\frac{d\hat{\boldsymbol{x}}}{dt} = \boldsymbol{F}_{\boldsymbol{x}}\hat{\boldsymbol{x}} + \begin{bmatrix}\dfrac{\partial \boldsymbol{f}}{\partial v_1} & \dfrac{\partial \boldsymbol{f}}{\partial v_2}\end{bmatrix}\begin{bmatrix}\hat{v}_1\\ \hat{v}_2\end{bmatrix} \tag{16}$$

where

$$\hat{\boldsymbol{x}} = \begin{bmatrix}\hat{a}_1\\ \hat{\theta}_1\\ \hat{a}_2\\ \hat{\theta}_2\end{bmatrix} \tag{17}$$

$$\boldsymbol{F}_{\boldsymbol{x}} = \begin{bmatrix}\dfrac{\partial f_1}{\partial a_1} & \dfrac{\partial f_1}{\partial \theta_1} & \dfrac{\partial f_1}{\partial a_2} & \dfrac{\partial f_1}{\partial \theta_2}\\ \dfrac{\partial f_2}{\partial a_1} & \dfrac{\partial f_2}{\partial \theta_1} & \dfrac{\partial f_2}{\partial a_2} & \dfrac{\partial f_2}{\partial \theta_2}\\ \dfrac{\partial f_3}{\partial a_1} & \dfrac{\partial f_3}{\partial \theta_1} & \dfrac{\partial f_3}{\partial a_2} & \dfrac{\partial f_3}{\partial \theta_2}\\ \dfrac{\partial f_4}{\partial a_1} & \dfrac{\partial f_4}{\partial \theta_1} & \dfrac{\partial f_4}{\partial a_2} & \dfrac{\partial f_4}{\partial \theta_2}\end{bmatrix}. \tag{18}$$

The equivalent circuit of the small signal model is shown in Fig. 5. According to (15), the small signals of the port currents are

$$\begin{cases}\hat{i}_1 = \nabla g_1\hat{\boldsymbol{x}}\\ \hat{i}_2 = \nabla g_2\hat{\boldsymbol{x}}\end{cases} \tag{19}$$

where the gradient of g_n $(n = 1, 2)$ is given by

$$\nabla g_n = \begin{bmatrix}\dfrac{\partial g_n}{\partial a_1} & \dfrac{\partial g_n}{\partial \theta_1} & \dfrac{\partial g_n}{\partial a_2} & \dfrac{\partial g_n}{\partial \theta_2}\end{bmatrix}. \tag{20}$$

C. Conductance Network Model

Based on (16) and (19), the transfer functions of voltages to currents are derived out

$$\begin{aligned}\boldsymbol{G}(s) &= \begin{bmatrix}\dfrac{\hat{i}_1(s)}{\hat{v}_1(s)} & \dfrac{\hat{i}_1(s)}{\hat{v}_2(s)}\\ \dfrac{\hat{i}_2(s)}{\hat{v}_1(s)} & \dfrac{\hat{i}_2(s)}{\hat{v}_2(s)}\end{bmatrix} x\\ &= \begin{bmatrix}\nabla g_1\\ \nabla g_2\end{bmatrix}(s\boldsymbol{I} - \boldsymbol{F}_{\boldsymbol{x}})^{-1}\begin{bmatrix}\dfrac{\partial \boldsymbol{f}}{\partial v_1} & \dfrac{\partial \boldsymbol{f}}{\partial v_2}\end{bmatrix}.\end{aligned} \tag{21}$$

This equation can be further simplified by neglecting the dynamics when the response speed of the WPT stage is fast enough and the latency is negligible. In mathematics, this condition means all the eigenvalues of $\boldsymbol{F}_{\boldsymbol{x}}$ have modulus that is much larger than the concerned angular frequency. With this simplification, a conductance network model is proposed and shown in Fig. 6, where the conductances and transconductances are given by

$$\begin{bmatrix}G_{11} & G_{12}\\ G_{21} & G_{22}\end{bmatrix} = \boldsymbol{G}(0) = -\begin{bmatrix}\nabla g_1\\ \nabla g_2\end{bmatrix}\boldsymbol{F}_{\boldsymbol{x}}^{-1}\begin{bmatrix}\dfrac{\partial \boldsymbol{f}}{\partial v_1} & \dfrac{\partial \boldsymbol{f}}{\partial v_2}\end{bmatrix}. \tag{22}$$

IV. System Level Modeling

Using the WPT stage models, we can simply develop a system level model by combining one of (12), (16), and (22) with the differential equations of the rest components of a WPT system. In this section, an open-loop WPT system and a preregulation WPT system are taken as examples to demonstrate the system level modeling method based on the WPT stage models.

A. Averaged Modeling of the Open-Loop WPT System

The circuit diagram of the open-loop WPT system is shown in Fig. 7. The WPT stage is directly powered by the system's dc input voltage v_{in}. The system's output voltage v_o is filtered by a capacitor C_f. The load is represented by a resistor R_L. It is worth noting that a battery can be simply modeled by a huge capacitor C_f in parallel with a resistor R_L during charging, and, therefore, the circuit diagram of Fig. 7 is also valid for battery charging system. Actually, the configuration of C_f and R_L is a very general model for dc powered load.

In Fig. 7, the energy storage element C_f is described by an additional differential equation

$$C_f\frac{dv_2}{dt} = -i_2 - \frac{v_2}{R_L}. \tag{23}$$

A fifth-order averaged model of this system is developed by combining (23) with (12) and substituting (15) into (23):

$$\begin{cases}\dfrac{d\boldsymbol{x}}{dt} &= \boldsymbol{f}(\boldsymbol{x}, v_1, v_2)\\ \dfrac{dv_2}{dt} &= \dfrac{1}{C_f}\left[-g_2(\boldsymbol{x}) - \dfrac{v_2}{R_L}\right]\end{cases} \tag{24}$$

where

$$\begin{cases}v_1 = v_{\text{in}}\\ v_2 = v_o.\end{cases} \tag{25}$$

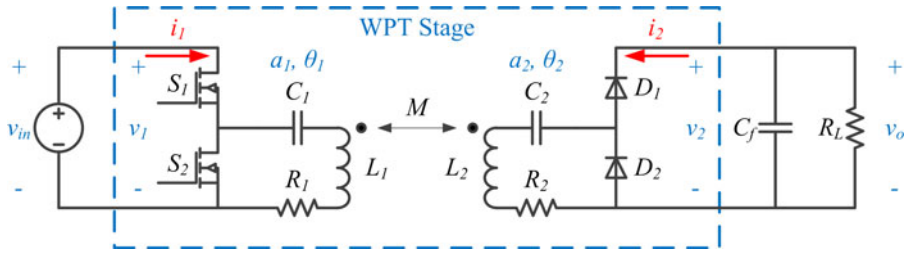

Fig. 7. Circuit diagram of the open-loop WPT system.

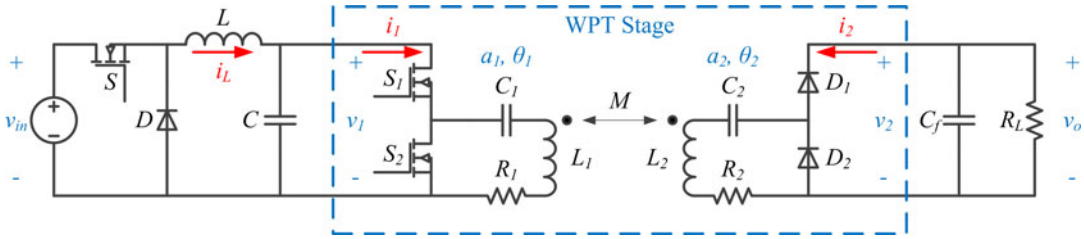

Fig. 8. Circuit diagram of the preregulation WPT system.

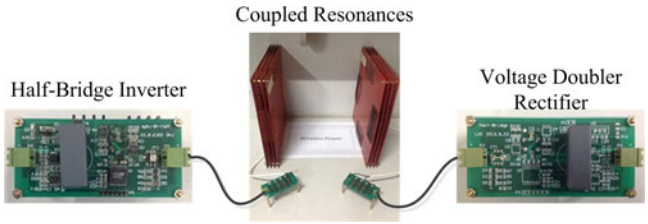

Fig. 9. WPT stage of the laboratory prototype.

B. Small Signal Modeling of the Preregulation WPT System

The circuit diagram of the preregulation WPT system is shown in Fig. 8. A buck converter is inserted to preregulate the input voltage of the WPT stage so that the transmitting side resonant current or the system's output voltage can be controlled. There are two energy storage elements in the buck converter: inductor L and capacitor C.

The small signal model of the buck converter is given by (26) when operating in continuous-conduction mode (CCM)

$$\frac{d}{dt}\begin{bmatrix}\hat{i}_L\\ \hat{v}_1\end{bmatrix}=\begin{bmatrix}0 & -\frac{1}{L}\\ \frac{1}{C} & 0\end{bmatrix}\begin{bmatrix}\hat{i}_L\\ \hat{v}_1\end{bmatrix}+\begin{bmatrix}0 & \frac{\bar{d}}{L} & \frac{\bar{v}_{in}}{L}\\ -\frac{1}{C} & 0 & 0\end{bmatrix}\begin{bmatrix}\hat{i}_1\\ \hat{v}_{in}\\ \hat{d}\end{bmatrix} \tag{26}$$

where $\hat{i}_L$ and $\hat{v}_1$ are the small signals of inductor current i_L and capacitor voltage v_1, respectively; $\hat{v}_{\rm in}$ is the small signal perturbation of input voltage; $\hat{d}$ is the small signal of the duty cycle of switch S; $\bar{v}_{\rm in}$ and $\bar{d}$ are the steady-state input voltage and duty cycle, respectively. The small signal expression of (23) is

$$\frac{d\hat{v}_2}{dt}=-\frac{1}{C_f}\hat{i}_2-\frac{\hat{v}_2}{C_f R_L}. \tag{27}$$

A seventh-order small signal model of this system is developed by combining (26) and (27) with (16) and substituting (19) into (26) and (27)

$$\frac{d}{dt}\begin{bmatrix}\hat{\boldsymbol{x}}\\ \hat{v}_1\\ \hat{v}_2\\ \hat{i}_L\end{bmatrix}=\begin{bmatrix}\boldsymbol{F_x} & \frac{\partial \boldsymbol{f}}{dv_1} & \frac{\partial \boldsymbol{f}}{dv_2} & \boldsymbol{0}\\ -\frac{\nabla g_1}{C} & 0 & 0 & \frac{1}{C}\\ -\frac{\nabla g_2}{C_f} & 0 & -\frac{1}{R_L C_f} & 0\\ \boldsymbol{0} & -\frac{1}{L} & 0 & -\frac{R}{L}\end{bmatrix}\begin{bmatrix}\hat{\boldsymbol{x}}\\ \hat{v}_1\\ \hat{v}_2\\ \hat{i}_L\end{bmatrix}+\begin{bmatrix}\boldsymbol{0} & \boldsymbol{0}\\ \frac{\bar{d}}{L} & \frac{\bar{v}_{in}}{L}\end{bmatrix}\begin{bmatrix}\hat{v}_{in}\\ \hat{d}\end{bmatrix} \tag{28}$$

where

$$v_2=v_o. \tag{29}$$

The steady-state operating point can be solved either by setting the large signal differential equations to zeros or by using the fundamental harmonic analysis.

The reduced order system based on the conductance network model is also developed by combining (26) and (27) with (22)

$$\frac{d}{dt}\begin{bmatrix}\hat{v}_1\\ \hat{v}_2\\ \hat{i}_L\end{bmatrix}=\begin{bmatrix}-\frac{G_{11}}{C} & -\frac{G_{12}}{C} & \frac{1}{C}\\ -\frac{G_{21}}{C_f} & -\frac{G_{22}}{C_f}-\frac{1}{R_L C_f} & 0\\ -\frac{1}{L} & 0 & 0\end{bmatrix}\begin{bmatrix}\hat{v}_1\\ \hat{v}_2\\ \hat{i}_L\end{bmatrix}+\begin{bmatrix}\boldsymbol{0} & \boldsymbol{0}\\ \frac{\bar{d}}{L} & \frac{\bar{v}_{in}}{L}\end{bmatrix}\begin{bmatrix}\hat{v}_{in}\\ \hat{d}\end{bmatrix} \tag{30}$$

TABLE I
PARAMETERS OF THE WPT STAGE

Symbol	Quantity	Value
L_1	transmitting side resonant inductance	136 μH
C_1	transmitting side resonant capacitance	0.75 nF
f_1	transmitting side resonant frequency	498 kHz
R_1	transmitting side ESR	1.5 Ω
L_2	receiving side resonant inductance	129 μH
C_2	receiving side resonant capacitance	0.75 nF
f_2	receiving side resonant frequency	512 kHz
R_2	receiving side ESR	1.5 Ω
M	mutual inductance	5.56 μH
f_s	switching frequency of the inverter	512.8 kHz
T_d	dead time of the inverter	100 ns

where

$$v_2 = v_o. \tag{31}$$

V. VALIDATION OF THE MODELS

In this section, the dynamic behaviors of a WPT laboratory prototype are examined in both time domain and frequency domain to validate the proposed models. The WPT stage of the laboratory prototype is shown in Fig. 9. Its parameters are listed in Table I, where the ESRs are estimated using the measured ac resistance of the coupled resonances, the drain-to-source on-time resistance of the MOSFETs, and the forward voltage and current of the rectifier diodes. The value of mutual inductance is calculated using Ansoft Maxwell 15 when the power transfer distance is 24 cm (the outer loop diameters of the coils are both 27 cm).

A. Validation of the Averaged Model

In order to examine the averaged model, we construct an open-loop WPT system as shown in Fig. 7 by connecting the WPT stage with a dc voltage supply (50 V), a filter capacitor (2.2 μF), and a load resistor (100 Ω). The waveforms of the resonant currents are measured when the inverter starts to operate and shown in Fig. 10(a). They are in agreement with the waveforms predicted by the averaged model of (24), as shown in Fig. 10(b). In contrast, the predicted waveforms without considering the dead time shown in Fig. 10(c) do not match the experimental results well. Therefore, the dead time is not ignorable in the startup process. The reason we explained in Section II.A is also proved by the phases shown in Fig. 10(b) and (c).

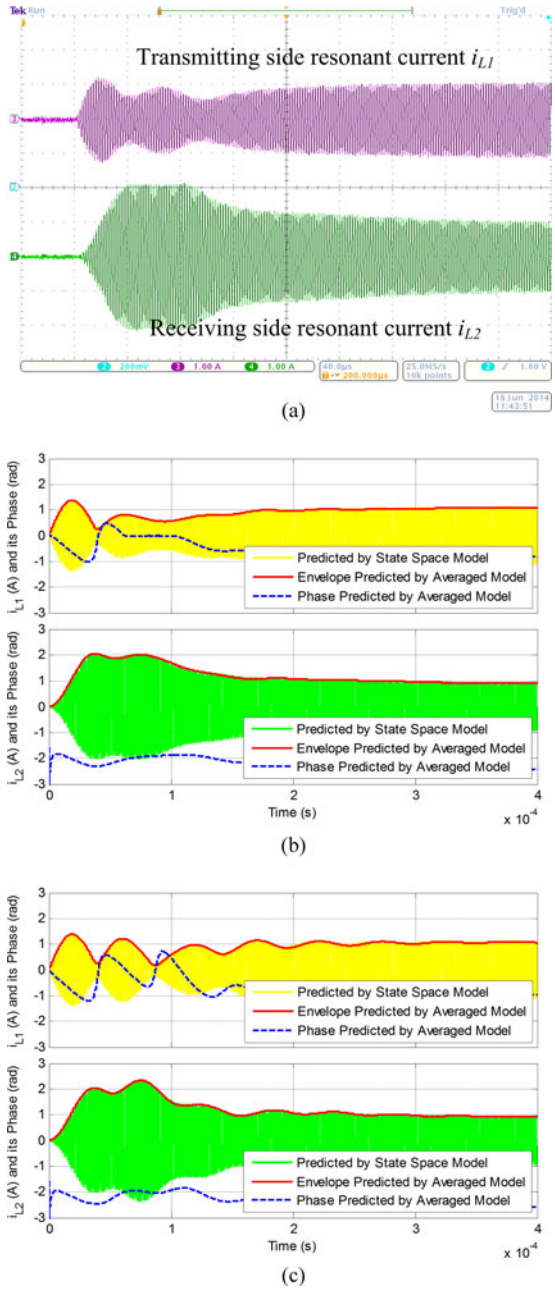

Fig. 10. Waveforms of the resonant currents in startup process of the open-loop WPT laboratory prototype. (a) Measured in experiment, (b) predicted by models, and (c) predicted without considering the dead time.

B. Validation of the Small Signal Model and the Conductance Network Model

In order to examine the small signal model and the conductance network model, we construct a preregulation WPT system as shown in Fig. 8 by inserting a buck converter into the open-loop WPT laboratory prototype. The system's input voltage is fixed at 100 V. The inductor and the capacitor of the buck converter are 780 and 4.4 μF, respectively. The buck converter is driven by a digital sinusoidal pulse width modulation (SPWM) wave with a switching frequency of 200 kHz. The average, minimum, and maximum duty cycles of the SPWM wave are 0.5, 0.49, and 0.51, respectively. Fig. 11 shows the ripple of the system's output voltage relative to the start signal of the SPWM wave so that both the magnitude and phase of control-to-output transfer function can be measured at each SPWM frequency. The control-to-output Bode diagram is obtained by sweeping the SPWM frequency and is plotted in Fig. 12, where it is also compared with the curves predicted by the small signal model and the conductance network model. The comparison result shows that the Bode diagram predicted by the small signal model is in agreement with the experimental results, and the

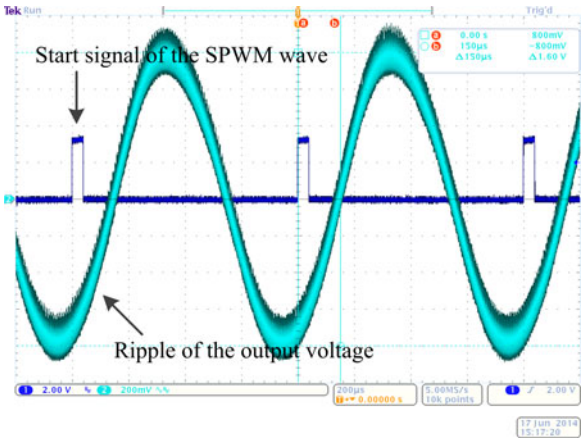

Fig. 11. Ripple of the system's output voltage relative to the start signal of the SPWM wave at 1.25 kHz.

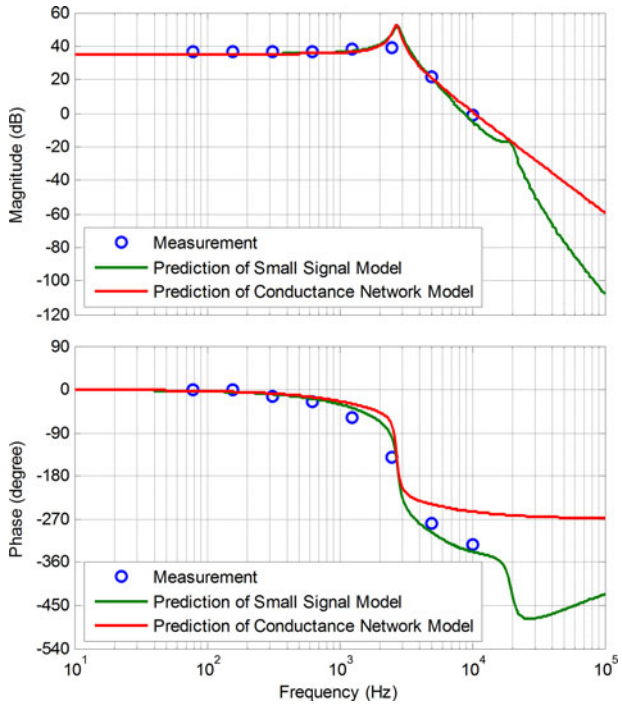

Fig. 12. Control-to-output Bode plots of the pre-regulation WPT laboratory prototype.

conductance network model provides a good tradeoff between accuracy and simplicity.

Although we may not use preregulation to control the system's output voltage in practice because it involves wireless communication and, therefore, additional latency, we can still use the preregulation WPT system to validate our models. The control-to-output Bode diagram gives a firm support to the proposed models because all the inertial elements of the system are included.

VI. Conclusion

The modeling method proposed in this paper is able to model the dynamics of an overall WPT system, including the inverter and rectifier. The modeling method is unique and prominent in that it considers a second-order resonator as a whole and takes the amplitudes and phases of the coupled modes as state variables. The orders of the proposed models are equal to or lower than that of the discrete state space model. The averaged model is accurate in large signal analysis when the dead time of the inverter is considered. The small signal model allows closed form analytical expressions to be developed for designing controllers. The conductance network model provides a good tradeoff between accuracy and simplicity. Definitely, the proposed modeling method applies to the resonant systems which consist of loosely coupled resonators, such as second-order resonant converters (consist of only one resonator), WPT systems with relay resonators, and wireless domino-resonator systems.

References

[1] J. Garnica, R. A. Chinga, and J. Lin, "Wireless power transmission: From far field to near field," *Proc. IEEE*, vol. 101, no. 6, pp. 1321–1331, Jun. 2013.

[2] S. Y. Hui, "Planar wireless charging technology for portable electronic products and Qi," *Proc. IEEE*, vol. 101, no. 6, pp. 1290–1301, Jun. 2013.

[3] Y. Hori, "Novel EV society based on motor/capacitor/wireless-application of electric motor, supercapacitors, and wireless power transfer to enhance operation of future vehicles," in *Proc. IEEE MTS-S Int. Microw.ave Workshop Ser. Innovative Wireless Power Transmiss.: Technol., Syst. Appl.* , May 2012, pp. 3–8.

[4] C. Wang, O. H. Stielau, and G. A. Covic, "Design considerations for a contactless electric vehicle battery charger," *IEEE Trans. Ind. Electron.*, vol. 52, no. 5, pp. 1308–1314, Oct. 2005.

[5] J. Sallán, J. L. Villa, A. Llombart, and J. F. Sanz, "Optimal design of ICPT systems applied to electric vehicle battery charge," *IEEE Trans. Ind. Electron.*, vol. 56, no. 6, pp. 2140–2149, Jun. 2009.

[6] H. Hao, G. A. Covic, and J. T. Boys, "An approximate dynamic model of LCL-T based inductive power transfer power supplies," *IEEE Trans. Power Electron.*, vol. 29, no. 10, pp. 5554–5567, Oct. 2014.

[7] S. Lee, B. Choi, and C. T. Rim, "Dynamics characterization of the inductive power transfer system for online electric vehicles by laplace phasor transform," *IEEE Trans. Power Electron.*, vol. 28, no. 12, pp. 5902–5909, Dec. 2013.

[8] P. Si, A. P. Hu, S. Malpas, and D. Budgett, "A frequency control method for regulating wireless power to implantable devices," *IEEE Trans. Biomed. Circuits Syst.*, vol. 2, no. 1, pp. 22–29, Mar. 2008.

[9] B. H. Waters, A. P. Sample, P. Bonde, and J. R. Smith, "Powering a ventricular assist device (VAD) with the free-range resonant electrical energy delivery (FREE-D) system," *Proc. IEEE*, vol. 100, no. 1, pp. 138–149, Jan. 2012.

[10] R. Xue, K. Cheng, and M. Je, "High-efficiency wireless power transfer for biomedical implants by optimal resonant load transformation," *IEEE Trans. Circuits Syst.-I, Reg. Papers*, vol. 60, no. 4, pp. 867–874, Apr. 2013.

[11] D. Ahn and S. Hong, "Wireless power transmission with self-regulated output voltage for biomedical implant," *IEEE Trans. Ind. Electron.*, vol. 61, no. 5, pp. 2225–2235, May 2014.

[12] A. P. Sample, D. A. Meyer, and J. R. Smith, "Analysis, experimental results, and range adaptation of magnetically coupled resonators for wireless power transfer," *IEEE Trans. Ind. Electron.*, vol. 58, no. 2, pp. 544–554, Feb. 2011.

[13] Y. Moriwaki, T. Imura, and Y. Hori, "Basic study on reduction of reflected power using dc/dc converters in wireless power transfer system via magnetic resonant coupling," in *Proc. IEEE 33rd Int.* Telecommun. *Energy Conf.*, Oct. 2011, pp. 1–5.

[14] N. Y. Kim, K. Y. Kim, J. Choi, and C. W. Kim, "Adaptive frequency with power-level tracking system for efficient magnetic resonance wireless power transfer," *Electron. Lett.*, vol. 48, no. 8, pp. 452–454, Apr. 2012.

[15] T. C. Beh, M. Kato, T. Imura, S. Oh, and Y. Hori, "Automated impedance matching system for robust wireless power transfer via magnetic resonance coupling," *IEEE Trans. Ind. Electron.*, vol. 60, no. 9, pp. 3689–3698, Sep. 2013.

[16] J. Yin, D. Lin, C. K. Lee, and S. Y. Hui, "Load monitoring and output power control of a wireless power transfer system without any wireless communication feedback," in *Proc. IEEE Energy Convers. Congr. Expo.*, Sep. 2013, pp. 4934–4939.

[17] W. Zhang, S. C. Wong, C. K. Tse, and Q. Chen, "Design for efficiency optimization and voltage controllability of series-series compensated inductive power transfer systems," *IEEE Trans. Power Electron.*, vol. 29, no. 1, pp. 191–200, Jan. 2014.
[18] H. Li, J. Li, K. Wang, W. Chen, and X. Yang. (2014). A maximum efficiency point tracking control scheme for wireless power transfer systems using magnetic resonant coupling *IEEE Trans. Power Electron.*, [Online]. Available: http://ieeexplore.ieee.org/stamp/stamp.jsp?tp = arnumber = 6880373
[19] A. K. Swain, M. J. Neath, U. K. Madawala, and D. J. Thrimawithana, "A dynamic model for bi-directional inductive power transfer systems," in *Proc. IEEE 37th Annu. Conf. Ind. Electron. Soc.*, Nov. 2011, pp. 1024–1029.
[20] A. K. Swain, M. J. Neath, U. K. Madawala, and D. J. Thrimawithana, "A dynamic multivariable state-space model for bidirectional inductive power transfer systems," *IEEE Trans. Power Electron.*, vol. 27, no. 11, pp. 4772–2780, Nov. 2012.
[21] A. P. Hu, "Modeling a contactless power supply using GSSA method," in *Proc. IEEE Int. Conf. Ind. Technol.*, Feb. 2009, pp. 1–6.
[22] Z. U. Zahid, Z. Dalala, and J. Lai, "Small-signal modeling of series-series compensated induction power transfer system," in *Proc. IEEE 29th Annu. Appl. Power Electron. Conf. Expo.*, Mar. 2014, pp. 2847–2853.
[23] H. A. Haus and W. Huang, "Coupled-mode theory," *Proc. IEEE*, vol. 79, no. 10, pp. 1505–1518, Oct. 1991.
[24] A. Kurs, A. Karalis, R. Moffatt, J. D. Joannopoulos, P. Fisher, and M. Soljačić, "Wireless power transfer via strongly coupled magnetic resonances," *Science*, vol. 317, no. 5834, pp. 83–86, Jul. 2007.
[25] H. Li, X. Yang, K. Wang, and X. Dong, "Study on efficiency maximization design principles for wireless power transfer system using magnetic resonant coupling," in *Proc. ECCE Asia Downunder*, Jun. 2013, pp. 888–892.

Hongchang Li (S'12) was born in Luoyang, China, in 1991. He received the B.S. degree in electrical engineering from Xi'an Jiaotong University, Xi'an, China, in 2011, where he is currently working toward the Ph.D. degree in electrical engineering..

His current research interests include wireless power transfer and digital control techniques.

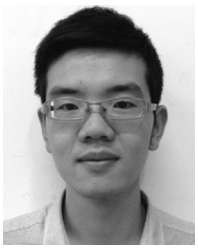

Kangping Wang (S'14) was born in Shaanxi, China, in 1989. He received the B.S. degree in electrical engineering from Xi'an Jiaotong University, Xi'an, China, in 2012, where e is currently working toward the Ph.D. degree in electrical engineering.

His current research interests include power electronic integration and packaging technologies.

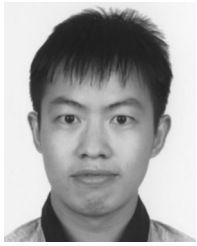

Lang Huang (S'14) was born in Chongqing, China, in 1988. He received the B.S. degree in electrical engineering from Xi'an Jiaotong University, Xi'an, China, in 2011, where he is currently working toward the Ph.D. degree in electrical engineering..

His current research interests include the control and topology of modular multilevel cascaded converter, and the high-precision waveform control.

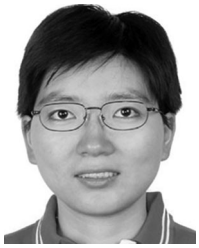

Wenjie Chen (S'06–M'08) received the B.S., M.S., and Ph.D. degrees in electrical engineering from Xi'an Jiaotong University, Xi'an, China, in 1996, 2002, and 2006, respectively.

Since 2002, she has been a Member of the Faculty of School of Electrical Engineering, Xi'an Jiaotong University, where she is currently a Professor. From January 2012 to January 2013, she was with the Department of Electrical Engineering and Computer Science, University of Tennessee, Knoxville, TN, USA, as a Visiting Scholar. She then came back to Xi'an Jiaotong University, and engaged in the teaching and researches in power electronics. Her main research interests include electromagnetic interference, active filters, and power electronic integration.

Xu Yang (M'02) received the B.S. and Ph.D. degrees in electrical engineering from Xi'an Jiaotong University, Xi'an, China, in 1994 and 1999, respectively.

Since 1999, he has been a Member of the Faculty of School of Electrical Engineering, Xi'an Jiaotong University, where he is currently a Professor. From November 2004 to November 2005, he was with the Center of Power Electronics Systems, Virginia Polytechnic Institute and State University, Blacksburg, VA, USA, as a Visiting Scholar. He then came back to Xi'an Jiaotong University, and engaged in the teaching and researches in power electronics and industrial automation area. His research interests include soft switching topologies, PWM control techniques and power electronic integration, and packaging technologies.